Biosensors and Bioelectronics 289 (2025) 117897

Contents lists available at ScienceDirect

Biosensors and Bioelectronics

journal homepage: www.elsevier.com/locate/bios

A SERS-active plasmonic nanosensor-chemometrics platform reveals a biphasic zinc switch that controls breast-cancer metastasis

Ting Zhou [a], Suliany Rodríguez-Barrios [b], Itziar Ruisánchez [b], Pilar Rivera-Gil [a,*]

[a] Integrative Biomedical Materials and Nanomedicine Laboratory, Medicine and Life Sciences Department, Universitat Pompeu Fabra, Carrer Del Doctor Aiguader 88, 08003, Barcelona, Spain

[b] Chemometrics and Sensorics for Analytical Solutions (CHEMOSENS) Group, Department of Analytical and Organic Chemistry, Rovira I Virgili University, Marcel·lí Domingo S/n, 43007, Tarragona, Spain

ARTICLE INFO

Keywords:
Labile zinc
Breast neoplasms-metastasis
Gold-silica nanocapsules
Raman spectroscopy-SERS
Plasmonic nanosensor
Multivariate calibration (partial least-squares chemometrics)
Intracellular ion sensing

ABSTRACT

Labile Zn^{2+} is emerging as a quantitative driver, not just a biomarker, of metastasis, yet rapid, second-resolved intracellular measurement remains elusive. Here we engineer terpyridine-functionalised, hollow Au@SiO_2 nanocapsules (NCs@TPY) and couple their SERS signal to cell-specific partial-least-squares (PLS) chemometrics, yielding an 8-log dynamic range (10^{-12} – 10^{-4} M), a low-nanomolar detection limit and ≤4.5 % cross-validated error while rejecting Ca^{2+}/Mg^{2+} interference. Applying this platform to four breast-cancer lines reveals that basal cytosolic Zn^{2+} forms a "ladder" paralleling metastatic aggressiveness (MCF-7 25 pM < MDA 430 pM < LM2 4.7 nM < BrM2 51 nM). Manipulating extracellular zinc uncovers a biphasic switch: migration, invasion and proliferation all peak when intracellular Zn^{2+} rises into the nanomolar band (~10–560 nM) and collapse once it exceeds ~5–70 μM (line-specific). Primary-tumour-derived MDA cells are hypersensitive, reaching maximal metastatic traits at ~0.6 μM Zn^{2+}, whereas lung- and brain-tropic variants show partial resistance, indicating micro-environmental adaptation. The NCs@TPY-PLS assay thus provides the first tool to track intracellular zinc across eight orders of magnitude *in situ* and demonstrates that tightly regulated Zn^{2+} dyshomeostasis controls metastatic behaviour. Because the Raman ligand is exchangeable, the capsule architecture is readily extendable to multiplex ion or redox sensing, and the identified "functional window" positions zinc transporters as actionable targets for anti-metastatic therapy.

1. Introduction

Metastasis is responsible for more than 90 % of cancer deaths and still lacks real-time biomarkers that can predict, monitor, or therapeutically exploit the transition from local growth to distant spread. Global statistics recorded 331 722 new breast-cancer cases and 58 667 deaths in 2022, with virtually all fatalities attributed to metastatic disease (GLOBOCAN, 2022). Even in the era of immune-checkpoint inhibition, the five-year survival for patients presenting with distant metastases remains below 30 % (Seyfried and Huysentruyt, 2013). Research over the past decade has revealed that metastatic competence is not governed solely by hard-wired genetic lesions but also by rapid, reversible changes in intracellular ion homeostasis, redox balance and mechano-signalling. Among these factors, **labile ("free") zinc (Zn^{2+})** has attracted special attention because it integrates metabolic status with transcriptional and enzymatic control yet fluctuates on the second-to-minute scale, much faster than conventional gene-expression readouts (Finney and O'Halloran, 2003).

Zinc's signalling role stems from its borderline Lewis-acid nature and tetrahedral coordination chemistry, which allow transient binding to histidyl and cysteinyl motifs in kinases, transcription factors and caspases. An estimated 10 % of the human proteome requires Zn^{2+} for structural integrity or catalysis (Colvin et al., 2010). In non-excitable mammalian cells, resting free Zn^{2+} in the cytosol is buffered to the 10^{-12} - 10^{-9} M range, three to six orders of magnitude below total cellular zinc (Finney and O'Halloran, 2003). Small upward excursions into the low-nanomolar band activate metal-responsive transcription factor 1 (MTF-1), whereas micromolar pulses trigger MAPK and NF-κB cascades and modulate matrix-metalloproteinases (Akhlaghipour and Moghbeli, 2024; Alam and Kelleher, 2012). Precisely because the

This article is part of a special issue entitled: Biosensors for Medicine published in Biosensors and Bioelectronics.

* Corresponding author.
E-mail address: pilar.rivera@upf.edu (P. Rivera-Gil).

https://doi.org/10.1016/j.bios.2025.117897
Received 25 April 2025; Received in revised form 12 July 2025; Accepted 16 August 2025
Available online 22 August 2025
0956-5663/© 2025 The Authors. Published by Elsevier B.V. This is an open access article under the CC BY-NC license (http://creativecommons.org/licenses/by-nc/4.0/).

dynamic window is so wide, quantitative tracking of intracellular Zn^{2+} has become a litmus test for next-generation biosensors.

Cancer cells frequently rewrite zinc homeostasis. In prostate, pancreatic and oesophageal tumours cytosolic Zn^{2+} falls, apparently to avoid mitochondrial overload, but in breast cancer the trend is reversed: malignant cells and their stromal niche accumulate zinc as malignancy progresses (Chandler et al., 2016; Kagara et al., 2007). A large-scale screen of 526 breast tumours linked high ZIP6/ZIP10 transporter expression to poor prognosis and lymph-node involvement (Taylor et al., 2016). Independent single-cell work confirmed that luminal A-type MCF-7 cells maintain sub-picomolar free Zn^{2+}, whereas triple-negative MDA-MB-231 variants up-shift to the 10^{-8} – 10^{-7} M band (Vogel-González et al., 2021). Whether these differences merely *reflect* aggressiveness or actively *drive* it has remained contentious, largely because no tool could monitor Zn^{2+} continuously across its eight-log span inside living, migrating cells.

ZIP influx and ZnT efflux transporters, together with metallothionein buffers, set the balance between attomolar signalling pools and millimolar stores in secretory vesicles. ZIP6/ZIP10 heteromers, in particular, facilitate an epithelial-mesenchymal transition (EMT) loop by importing Zn^{2+} that activates STAT3, which in turn up-regulates ZIP expression (Taylor et al., 2016). Matrix-metalloproteinases 2 and 9 (MMP-2/-9) require micromolar Zn^{2+} for catalytic activity and liberate EMT-inducing growth factors from the extracellular matrix (Akhlaghipour and Moghbeli, 2024). Understanding how *absolute* cytosolic Zn^{2+} concentrations translate into migratory or invasive phenotypes therefore demands an assay that (i) spans at least 10^{-11} – 10^{-5} M, (ii) works rapid, second-resolved, and (iii) discriminates zinc from the millimolar Ca^{2+} and Mg^{2+} background of the cytosol.

Detecting changes in labile zinc can support diagnostics and inform targeted therapies, with molecular probes enabling sensitive measurement in biological systems. Current methodologies for quantifying intracellular zinc at subcellular levels remain inadequate, hindering a deeper understanding of how labile zinc fluctuations contribute to metastasis. Fluorescence-based zinc sensors, for example, have been widely used; however, they suffer from limitations such as photobleaching, low sensitivity, and poor spatial resolution, making them suboptimal for high-precision intracellular measurements (Carregal Romero et al.; Kantner et al., 2015). Fluorescent chelators such as FluoZin-3 or "Zinpyr" indicators offer nanomolar sensitivity but suffer from photobleaching, pH cross-talk and dye leakage (Maret, 2015). They also saturate above ≈100 nM and cannot distinguish overlapping emission bands when multiplexed. Electrochemical nano-electrodes push detection to the picomolar regime yet distort the intracellular milieu and are limited to single-point readouts (Ringgit et al., 2022).

Surface-enhanced Raman spectroscopy (SERS), by contrast, provides vibrational fingerprints that are inherently multiplexable and photostable (Tsoutsi et al., 2018). Noble metal nanostructures generate localised surface-plasmon resonances (LSPR) that amplify Raman scattering by six to eight orders of magnitude, enough to detect single molecules (Nie and Emory, 1997). Hollow Au@SiO_2 nanocapsules pioneered by Correa-Duarte and Liz-Marzán create stable, solvent-accessible "hot-spots" protected from biofouling (Rivera-Gil et al., 2013; Sanles-Sobrido et al., 2009; Vázquez-Vázquez et al., 2013). Later work exploited anisotropic CuTe nanocrystals (Li et al., 2013) and spread-spectrum encoding to achieve attomolar neurotransmitter detection in neurons (Lee et al., 2021).

SERS nanoprobes often incorporate a Raman-active reporter molecule whose vibrational pattern shifts upon binding. For example, pH-sensitive reporters (like 4-mercaptobenzoic acid or p-aminothiophenol) attached to gold nanostructures have been used to map subcellular pH values (García-Algar et al., 2017; Kneipp et al., 2010; Xiao et al., 2023). Our work shows that these SERS-active probes can enter cells, remain biocompatible, while allowing small molecules to diffuse to the SERS-active surface to provide dynamic spectroscopic readouts of biochemical events. For example, silica-coated gold nanoprobes functionalised with a NO-reactive monolayer were developed to quantitatively monitor nitric oxide inside lysosomes in real time, without perturbing cell viability (Rivera-Gil et al., 2013). In another example, we developed a multiplex nanosensor for pH and ROS. The nanocapsule's internal Au network effectively harnesses the plasmonic energy to both amplify Raman signals and drive the boronic probe's oxidative reaction. The result is sub-micromolar ROS specie, H_2O_2, detection limits and clear signal discrimination even for minor pH differences (Xiao et al., 2023). Such sensitivity is especially important for biosensing of signaling molecules like H_2O_2, which are often produced at low concentrations.

In the case of SERS nanosensors for zinc, 2,2′:6′,2″-Terpyridine (TPY) is attractive because it offers nanomolar Zn^{2+} affinity and a rich Raman signature (Šloufová et al., 2018). Zhou et al. recently grafted TPY onto silica-coated Au clusters and monitored Zn^{2+} in metastatic breast-cancer cells, but the sensor covered <2 orders of magnitude and used a single 1021 cm^{-1}/1108 cm^{-1} intensity ratio, making it vulnerable to Ca^{2+}/Mg^{2+} or pH cross-talk (Zhou et al., 2024). Eremina et al. improved solution-phase selectivity by chemisorbing TPY on Ag nanoparticles in freshwater samples, yet intracellular quantification remained out of reach (Eremina et al., 2024). Clearly missing is a strategy that *combines hotspot-rich nanostructures with multivariate calibration* capable of de-convoluting zinc signals from spectral background inside live cells.

Chemometrics offers such a route. Partial-least-squares (PLS) regression reduces full Raman spectra to latent variables that capture covariance between predictor (spectra) and response (concentration) matrices, thereby minimizing errors from baseline drift or batch-to-batch nanostructure variance (dos Santos et al., 2023). Although machine-learning regressors such as support vector regression (SVR) and artificial neural networks (ANN) have been applied to vibrational spectroscopy in other contexts, particularly when very large calibration sets are available, partial least-squares (PLS) remains the recommended approach for small-to-moderate datasets of highly collinear spectra (Bro and Smilde, 2014). PLS offers transparent latent variables that can be linked to specific Raman bands and requires only a handful of hyper-parameters, making it especially suitable for intracellular SERS studies where interpretability and limited sample size are critical. Guided by this consensus, we adopted PLS as the chemometric core of the present Zn^{2+} calibration. Brackx et al. used PLS with SERS to quantify Zn^{2+} in river water, achieving a 10-fold lower root-mean-square error than univariate calibration (Brackx et al., 2020), but their colloidal sensor aggregated in cell culture and was never applied *in situ*.

Here we close that gap by integrating SERS-active nanocapsules with full-spectrum PLS chemometrics. We synthesise hollow Au@SiO_2 nanocapsules densely functionalised on the interior surface with TPY (NCs@TPY). The capsules preserve the LSPR of the encapsulated Au network at ≈780 nm, matching the low-phototoxicity window for near-infra-red excitation, and they present a mesoporous silica wall that permits Zn^{2+} diffusion while excluding macromolecular fouling. We then acquire full 400 - 1800 cm^{-1} spectra from NCs@TPY inside live cells across an external $ZnSO_4$ gradient (10^{-12} – 10^{-4} M) and build **cell-specific PLS models** for four breast-cancer lines that represent an aggressiveness gradient: low-metastatic MCF-7; highly invasive but organ-naïve MDA-MB-231 (MDA); lung-tropic LM2; and brain-tropic BrM2. Cross-validation reveals ≤4.5 % error over eight orders of magnitude and negligible interference from 1 mM Ca^{2+}/Mg^{2+}.

With the analytical tool in hand we ask two questions: (i) *Do basal cytosolic* Zn^{2+} *levels correlate with intrinsic metastatic potential?* and (ii) *Is there a quantitative* Zn^{2+} *threshold that actively modulates migration, invasion and proliferation?* Our data answer both in the affirmative. Basal Zn^{2+} indeed forms a "ladder": MCF-7 25 pM < MDA 430 pM < LM2 4.7 pM < BrM2 51 nM (all values refer to free cytosolic concentration calculated by PLS). When we titrate extracellular zinc, metastasis-related traits display a sharp **biphasic response**: migration, invasion and proliferation peak when intracellular Zn^{2+} enters the nanomolar

window (≈12–560 nM) and collapse in the low micromolar window depending on the cell type. MDA cells, derived from the primary tumour, reach maximal motility at ≈12–560 nM; LM2 and BrM2 are partially resistant, consistent with prior adaptation to lung or brain microenvironments; MCF-7 never acquires significant motility. The thresholds align with known half-maximal activities of ZIP6/10 influx (≈0.3–1 μM) and MMP-2/-9 catalysis (≈0.5–5 μM), suggesting that zinc is not merely a marker but a functional *switch* in the metastatic programme.

Beyond zinc biology, our work illustrates three general advances. First, the NCs@TPY architecture is modular: exchanging the terpyridine ligand for ferrocene, boronic acids or dithienyl-imidazoles enables real-time mapping of redox and pH gradients with the same plasmonic chassis. Second, full-spectrum chemometrics transforms SERS from a largely qualitative fingerprinting tool into a **quantitative** intracellular assay comparable in precision to fluorescence lifetime imaging yet without fluorophore drawbacks. Third, by combining intracellular metal sensing with functional phenotyping (migration/invasion assays, proliferation) in the *same* cellular system, we provide a framework for discovering concentration thresholds that translate biochemical signals into clinically relevant behaviour.

In summary, we present a SERS-active plasmonic nanosensor - chemometrics platform that (i) quantifies intracellular zinc across eight orders of magnitude with low-nanomolar sensitivity, (ii) reveals a biphasic Zn^{2+} switch that quantitatively controls metastatic behaviour, and (iii) is readily extendable to multiplex ion sensing. These findings not only clarify zinc's mechanistic role in breast-cancer dissemination but also position zinc transporters as actionable drug targets: pushing cytosolic Zn^{2+} below ≈10 nM or above ≈60 μM (cell specific) emerges as a tangible route to restrain metastasis. We anticipate that the platform can be deployed in patient-derived organoids and *in vivo* models to guide combination therapies that exploit metal-ion dyshomeostasis alongside molecular-targeted agents.

2. Materials and methods

2.1. Materials

450 nm polystyrene (PS) beads were purchased from Ikerlat. 2,2':6′,2″-Terpyridine-4′-Thiol (TPY) was purchased from ALFA Chemistry. Polyvinylpyrrolidone (PVP, MW: 10000), polysodium (styrene sulfonate) (PSS, MW: 70000), poly (allylamine hydrochloride) (PAH, MW: 50000), tetrakis (hydroxymethyl) phosphonium chloride solution (THPC), gold (III) chloride trihydrate, ammonia solution, tetraethyl orthosilicate (TEOS), phosphoric acid, sodium phosphate monobasic, sodium phosphate dibasic, crystal violet solution, acetic acid, zinc sulfate heptahydrate ($ZnSO_4{\cdot}7H_2O$), calcium chloride ($CaCl_2$) and zinquin were purchased from Sigma-Aldrich. Sodium hydroxide, Paraformaldehyde (PFA, 4 % in PBS) solution, cell counting chamber slide and CellTrace CFSE cell proliferation kit (containing CFSE reagent and DMSO, for flow cytometry) were purchased from ThermoFisher. Chloroform was purchased from Scharlau. Ibidi glass bottom dish (35 mm) was purchased from ibidi GmbH. Matrigel basement membrane matrix (Corning 356234) and Transwell insert (8 μm PET membrane, Corning 3464). All the chemicals were used without further purification.

2.2. Cell culturing and zinc supplementation

We worked with the brain-metastatic triple-negative breast cancer cell line MDA-MB-BrM2 (BrM2) and the lung-metastatic triple-negative breast cancer cell line MDA-MB-LM2 (LM2), both generously provided by Joan Massagué from the Memorial Sloan Kettering Cancer Center (New York, NY, USA), along with their parental cell line MDA-MB-231 (MDA), a well-known triple-negative breast cancer cell line. TNBC lacks estrogen receptors, progesterone receptors, and HER2, characteristics that contribute to its higher metastatic potential. For comparison, we included the MCF-7 cell line, which is non-invasive and has low metastatic potential, as a control group. MCF-7 is positive to estrogen and progesterone receptors (ER^+ and PR^+). To simplify the cell names within the manuscript, we used these abbreviations: MCF-7, MDA, LM2, BrM2.

Cells were cultured in Dulbecco's Modified Eagle Medium High Glucose with L-Glutamine without Sodium Pyruvate (DMEM High Glucose, Biowest), supplemented with 10 % fetal bovine serum (FBS) and 1 % penicillin-streptomycin, which was named as cell growth medium (GM). Cells were maintained at 37 °C in a humidified atmosphere with 5 % CO_2.

To prepare zinc-depleted GM, FBS was treated with Chelex 100 resin (Bio-Rad Laboratories, Hercules, CA, USA) according to the manufacturer's instructions to effectively remove divalent cations such as Zn^{2+}, Ca^{2+}, and Mg^{2+}. Chelex was applied solely to the FBS fraction; the underlying DMEM, which contains 1.8 mM $CaCl_2$ and 0.8 mM $MgSO_4$, was left untreated. Final Ca^{2+} and Mg^{2+} concentrations after chelexed-FBS addition were kept within normal physiological ranges. $ZnSO_4$ was subsequently added to the zinc-depleted medium to achieve the desired zinc concentrations.

The zinc-supplemented conditions were: standard GM containing 2 μM zinc (GM-2 μM, considered as the basal condition), zinc-depleted medium (0 μM zinc), and zinc-depleted medium supplemented with 10, 50, or 100 μM $ZnSO_4$.

Basal free Zn^{2+} in resting mammalian cytosol is < 1 nM (10^{-9} M) (Maret, 2017). Concentrations above ~10 nM trigger metal-responsive-element binding; ≥1 μM are considered 'stress-levels' that activate MAPK and NF-κB (Alam and Kelleher, 2012). Our supplementation steps therefore span the physiological (10^{-9} - 10^{-8} M) to the signalling (10^{-7} - 10^{-6} M) and supra-physiological ($>10^{-5}$ M) ranges.

2.3. Synthesis of Au@SiO_2 nanocapsules (NCs)

Au@SiO_2 nanocapsules (NCs) were synthesized following the method detailed in our previous work (Rivera-Gil et al., 2013; Xiao et al., 2023; Zhou et al., 2024). In summary, 450 nm polystyrene (PS) beads were used as templates and coated with layer-by-layer (LBL) polymers through electrostatic adsorption. Positively charged poly (allylamine hydrochloride) (PAH) and negatively charged poly (styrene sulfonate) (PSS) were alternately deposited onto the PS beads to form a dense outer PAH layer (PS@LBL). THPC-reduced gold seeds (3–5 nm) were then loaded onto the LBL-coated beads, providing nucleation sites for the subsequent growth of gold nanoparticles. Next, a mesoporous silica layer (~20 nm) was synthesized by combining polyvinylpyrrolidone (PVP) with tetraethyl orthosilicate (TEOS), resulting in PS@LBL@Auseeds@SiO_2. The PS cores were dissolved using an ethanol/chloroform (1:3 v/v) mixture, yielding hollow silica capsules (Hollow). To enhance the plasmonic efficiency of the nanostructure, gold nanoparticles were grown *in situ* on the Au seeds *via* catalysed reduction of gold ions with formaldehyde. After each step, the samples were washed three times to remove unbound reagents.

2.4. Synthesis of zinc-nanosensors and evaluation of their stability across various pH levels

TPY was selected as the Raman probe due to its excellent Raman cross-section and strong affinity for metal ions. To enhance the nanosensor's signal output, two key factors were systematically optimized: the conjugation time (1, 3, 6, 12, 24, 36, and 48 h) and the TPY concentration (50, 250, and 500 μM). Specifically, equal volumes (1 mL) of NCs were mixed with varying concentrations of TPY (1 mL) and incubated for different durations. Following the reaction, the samples were washed and centrifuged (4500 rpm, 10 min) 4 times with ethanol to remove the extra TPY. The samples were then thoroughly washed and resuspended in the appropriate medium before conducting SERS measurements.

To investigate the stability of the SERS signal across different pH levels, we prepared 100 mM phosphate buffers with pH values ranging from 3 to 9 using phosphoric acid, sodium phosphate monobasic, and sodium phosphate dibasic. We then added 500 μL of 0.5 mg/mL NCs@TPY to 500 μL of 500 μM TPY in each buffer at the specified pH levels (pH = 3, 4, 5, 6, 7, 8, 9) and incubated the mixtures for 3 h.

2.5. Physicochemical characterization

Transmission Electron Microscopy (TEM): TEM analysis was carried out with a JEOL JEM 1010 microscope at 80 kV. Samples were dispersed in ethanol, applied to copper grids (Formvar/Carbon-Supported, 200 mesh, TED PELLA INC., USA), and dried overnight at room temperature.

UV–Vis Spectroscopy: Absorption spectra of each synthetic step were recorded using a UV–Vis spectrometer (GE Healthcare Ultrospec 2100 pro) with a black quartz cuvette. Samples were scanned from 200 to 900 nm with water as the reference.

Dynamic Light Scattering (DLS): Hydrodynamic diameter and zeta potential were measured using a Zetasizer Nano ZS (Malvern Instruments, UK). Samples (0.02 mg/mL) were diluted in water. Disposable cuvettes (Sigma-Aldrich, Darmstadt, Germany) were used for size measurements, and folded capillary cells (Malvern Instruments, UK) for zeta potential. The refractive index was 0.2 and the absorption was 3.32. Each sample was measured three times with 10 runs per measurement.

A comprehensive suite of structural and compositional analyses for this nanocapsule platform, including high-resolution TEM/HRTEM, *in situ* SAXS, and STEM-EDX elemental mapping, has already been reported in detail in our previous publications (Rivera-Gil et al., 2013; Xiao et al., 2023) and related follow-up studies. Readers are referred to those works for exhaustive characterisation data that fully document the template to hollow to NC transformation.

Surface-Enhanced Raman Scattering (SERS): SERS measurements were taken using a Renishaw inVia Qontor Raman system with a 785 nm NIR laser and a 1200 l/mm grating. NCs@TPY samples were placed in glass-bottom dishes (ibidi), and the laser was focused on the NCs@TPY using a 60X water immersion objective (NA 1.00) with an approx. 1-μm laser spot diameter. The integration time was set to 1 s and the power at the sample to 0.35 mW. For each concentration gradient sample, each spectrum was the average of 5 spectra. Data was analyzed using Windows-based Raman Environment (WiRE) software.

2.6. SERS data acquisition and processing

For all experiments involving SERS measurements (univariate calibration, multivariate PLS modeling, and intracellular quantification), a minimum of five independent spectra were collected per condition. In univariate calibration, five replicate spectra were averaged into a single composite spectrum to generate each calibration point. For intracellular SERS measurements used in multivariate PLS models or biological assays, each of the five spectra per condition was retained as an individual datapoint without averaging, to preserve cell-to-cell variability. All spectra were recorded at random locations within the cytosol to avoid positional bias.

Pre-processing of the SERS data was carried out using Spyder (Anaconda3). To eliminate autofluorescence background, baseline correction was applied to the spectra using the asymmetric least squares smoothing algorithm (Peng et al., 2010). For each sample, SERS spectra were collected from five randomly selected points, and the average spectrum was then calculated for further analysis.

2.7. Methods for the quantification of zinc in unknown biological samples

We used two methodologies to build the calibration curve: (i) univariate calibration, and (ii) multivariate calibration. The former was done in solution and the latter in the cells. For both, we prepared solutions with different zinc amounts by adding 1 mM $ZnSO_4$ to the corresponding media. The obtained zinc concentrations ranged from 10^{-4}-10^{-12} M. For all cases, we used 0.25 mg/mL (calculated by the number of NCs) NCs@TPY.

Univariate calibration: We used zinc-depleted GM supplemented with 1 mM $ZnSO_4$ to obtain the solutions with different zinc amounts (from 10^{-4}-10^{-12} M). We added the NCs@TPY to the solutions, waited for 30 min, and performed the SERS measurements. Each sample was measured at least 5 times. We averaged the spectra and we analyzed the spectral variance across the concentration gradient. Based on this variance, peaks showing more than 25 % change were identified as zinc-sensitive peaks and less than 25 % as insensitive. We compared various combinations of intensity ratios between sensitive and insensitive peaks (Fig. SI–3). The logarithmic ratio of the intensity at 1021 cm^{-1} (I_{1021}, zinc-sensitive) to the intensity at 1108 cm^{-1} (I_{1108}, zinc-insensitive) emerged as the optimal model. This logarithmic ratio was plotted on the y-axis against the logarithmic zinc concentration on the x-axis to generate a calibration curve through linear regression fitting.

Multivariate calibration: The four cell lines were seeded at a cell density of 5×10^4 cells/mL onto glass bottom dishes (from Ibidi®) and were allowed to grow up to a cell density of 80 %–90 %. Then we exposed the cells to the NCs@TPY (0.25 mg/mL) for 24 h in zinc-depleted GM. We rinsed twice with PBS and incubated the cells in the zinc-depleted GM with different concentrations of zinc (from 10^{-4} M to 10^{-11} M, 2 mL) for 2 h. The acquisition of the SERS spectra was carried out immediately after the incubation. For each cell line, the dataset comprised a calibration set of 57 (MCF-7), 43 (MDA), 49 (LM2), and 51 (BrM2) spectra, with at least five replicates per Zn^{2+} concentration, and an independent prediction set of five additional samples.

Prior to model building we surveyed the regression methods most often recommended for quantitative vibrational spectroscopy. The consensus in the chemometric literature (Bro and Smilde, 2014) is that PLS balances predictive power, robustness to spectral collinearity and chemical interpretability, particularly when the number of independent samples is constrained by biological experimentation. Alternative non-linear techniques such as SVR and ANN were therefore considered outside the scope of the present exploratory study; they will be revisited once larger intracellular SERS datasets become available. All subsequent analyses in this work were performed with PLS, as detailed below.

A multivariate calibration model was established by partial least squares (PLS) regression, which captures the relationships between the SERS spectra (dependent variables) and the Zn^{2+} concentration (independent variable), while accounting for potential interferents from other cations in the sample matrix (such as Ca^{2+} and Mg^{2+}). A critical step in PLS model development is the selection of the optimal number of latent variables (LVs), which reduces spectral dimensionality while preserving relevant spectral variability associated with the analyte of interest. Cross-validation (CV), particularly ten-fold CV, was used to determine the optimal number of LVs (Wiklund et al., 2007). By integrating the full spectral profile, PLS enhances both accuracy and reliability of quantitative predictions, outperforming univariate approaches in complex biological matrices.

PLS models were carried out with Matlab (The MathWorks Inc., Natick, MA, R2022a) and PLS-Toolbox v7 (The Eigen Vector Research, Manson, WA).

A consolidated schematic that integrates the Raman-SERS measurement setup and the intracellular Zn^{2+} data-analysis workflow is provided in the Supplementary Information (Section “General Scheme”) for quick reference.

2.8. Cell proliferation

Cell proliferation was monitored over four days using CellTrace CFSE reagent (Ex/Em = 492/517 nm). After sufficient cell attachment (80–90 %), the four cell lines were harvested and resuspended into PBS at a concentration of 10^6 cells/mL. The CFSE stock solution was prepared immediately prior to use by adding 18 μL of DMSO to one vial of CFSE

reagent and mixed well to yield a 5 mM stock concentration. Next, we added 1 μL of CFSE stock solution to each mL of cell suspension in PBS to obtain a final working solution of 5 μM. The cells were incubated with the CFSE solution for 20 min at 37 °C in the dark. To remove any residual free dye, five times the original staining volume of GM was added to the cells, followed by a 5-min incubation. Cell suspensions were centrifuged (1200 rpm, 5 min) and the cell pellet was resuspended in fresh pre-warm complete GM. The cells were incubated for an additional 15 min before analysis to allow the CFSE reagent to undergo acetate hydrolysis. Then, 4×10^4 stained cells were seeded into a 12-well plate and each well contained different concentrations of zinc (0, 10, 50, 100 μM and regular GM containing 2 μM (GM-2 μM). The cells were harvested on different days (D0-D4) and resuspended to 0.5 mL PBS for analysis of fluorescence intensity. Fluorescence was quantified using an LSRII flow cytometer with a 488-nm excitation source. Further data analysis was performed using Flowing Software (Turku Bioscience, Turku, Finland). Here, we used the fluorescence intensity ratio of cells, which is the fluorescence intensity of daughter cells divided by the fluorescence intensity of their parent cells. The discrete peaks in the flow cytometer histogram represent the successive generations of cells, and cells of different generations show different peaks (Fig. SI–5). The mean value of the peaks is selected as the fluorescence intensity of cells of different generations. To better compare the proliferation between the different cells, their fluorescent intensities were normalized to basal condition (GM-2 μM). As cell proliferation occurs, the signal of the dye decreases. The legend colour from pink to violet represented the proliferation rate ranging from 1.43-0.56, respectively. The lower the ratio (color-coded in violet), the higher the dilution of the dye is, and the faster the proliferation rate is.

In parallel, we conducted a similar experiment, in which 0.25 mg/mL NCs@TPY was added to each well. SERS measurements were then performed to detect the actual zinc levels under different conditions across the four cell lines. At least five spectra were collected per sample from random locations inside the cell.

2.9. Zinc imbalance index (ZII) metrics

For each well and day we computed the normalized fluorescence ratio as mentioned before:

$$R_D = \frac{F_{D,test}}{F_{D,GM-2\mu M}}$$

Where $F_{D,\ test}$ is the median fluorescence of a zinc-treated well on day D, and $F_{D,\ GM\text{-}2\mu M}$ is the median of the GM-2 μM control on the same plate and day. Because CFSE fluorescence halves with each division, $R_D < 1$ signifies faster proliferation and $R_D > 1$ slower growth relative to the control. Then we calculated the increment of R_D to express the proportional change in proliferation for each day with respect to the GM-2μM reference:

$$\Delta R_D = R_D - 1$$

The ZII summarizes the growth effect over the four-day period:

$$ZII = \frac{1}{4}\sum_{D=1}^{4} \Delta R_D$$

positive ZII indicates net growth inhibition and negative ZII net growth stimulation. Pearson r was obtained by linear regression of ZII against $\log_{10}C_{Zn2+}$ measured after zinc exposure (Fig. 3B).

2.10. Cell migration and invasion

Cell migration refers to the movement of cells from one area to another, whereas cell invasion involves the penetration of cells through an extracellular matrix (ECM) barrier *via* enzymatic degradation. To study these processes, we used Corning's Transwell permeable supports, either coated with Matrigel matrix (Matrigel) for invasion assays, or left uncoated for migration assays, respectively. Following the manufacturer's introductions, we thawed the Matrigel basement membrane matrix on ice at 4 °C overnight to ensure it thawed completely. The Matrigel matrix was then diluted in DMEM basal medium to a final concentration of 200 μg/mL. We carefully added 100 μL of the diluted Matrigel matrix to the center of each Transwell insert for invasion assays, while inserts for migration assays were not coated. The plates were incubated at 37 °C for 1 h to allow the Matrigel matrix to form a gel.

The four cell lines were seeded into 6-well plates with different gradients of zinc (0, 10, 50, 100 μM and GM-2 μM) over 2 days until reaching 80–90 % confluency. Then, cells were trypsinized and resuspended in a serum-free medium at a concentration of 3×10^5 cells/mL. A 200 μL aliquot of each cell suspension with varying zinc concentrations was seeded into the upper chamber of each Transwell insert, achieving a final cell density of 6×10^4 cells/well. The lower chamber of each Transwell was filled with 800 μL of GM containing 10 % FBS as a chemoattractant. The cells were cultured in an incubator at 37 °C with 5 % CO_2. After 48 h of incubation, the cells remaining inside the Transwell inserts were removed. The cells on the lower surface of the membrane, which had migrated or invaded through the membrane, were fixed with PFA and stained with crystal violet for 10 min, respectively. The Transwell inserts were washed twice with PBS to remove unbound crystal violet and air-dried. The migrated and invaded cells were observed and imaged under a microscope and incubated for 48 h. Then we used crystal violet (CV) to stain the migrated and invaded cells, and the stain was subsequently eluted from the cells to measure their absorbance.

For the migration and invasion quantification, we added 400 μL of 33 % acetic acid into each insert and shacked for 10 min so that the bound crystal violet was eluted. A 100 μL aliquot of eluent from the lower chamber was transferred to a 96-well clear microplate, and the absorbance at 590 nm was measured using a plate reader. To generate a standard curve, the four cell lines were diluted in culture medium to a series of cell densities (0.5, 1.5, 3, 6, 9×10^6 cells) and seeded into 96-well microplate. The cells were cultured, stained, and quantified as described above. The standard curves of cell numbers versus absorbance were plotted.

To elucidate the relationship between the intracellular amount of zinc and the migratory and invasive abilities of different cell lines, we conducted a similar experiment. Each cell line was cultured in zinc-depleted GM with varying zinc additions for 2 days, after which 0.25 mg/mL NCs@TPY was added to each well. SERS measurements were then performed to determine the actual intracellular zinc levels under different conditions for the four cell lines. For each sample, five spectra were collected from random locations within the cell.

3. Results and discussions

3.1. Synthesis, characterization and stability assessment of plasmonic zinc nanosensors (NCs@TPY)

We synthesized the colloidal carrier (NCs) based on a methodology published by Correa-Duarte, Liz-Marzán et al. (Sanles-Sobrido et al., 2009; Rivera-Gil et al., 2013). We introduced modifications to enhance its plasmonic properties and colloidal stability (Xiao et al., 2023). The synthesis followed a layer-by-layer (LbL) assembly, where a trilayer of polymers (PAH@PSS@PAH) was deposited onto a negatively charged polystyrene (PS) template. Gold (Au) seeds were incorporated as part of this process. The outermost layer consisted of mesoporous silica (SiO_2), which acts as a selective barrier, allowing analytes to diffuse in while preventing biomolecular interactions with the plasmonic surface, thereby reducing noise. We then chemically removed the template; the bright center confirms removal of the PS template, leaving a hollow interior. Finally, we grew the Au seeds to form plasmonic nanoclusters (NCs), increasing the plasmonic surface area and optimizing the sensor's performance.

Compared with both the hollow stage and the less densely Au-decorated shells we previously reported (Zhou et al., 2024), the NC micrograph in Fig. 1A (and Fig. SI–1) shows higher electron contrast along the silica wall and a red shift in the localized surface plasmon resonance (LSPR) peak (Fig. 1B). This arises from Au over-growth that forms a continuous nanostructured layer, thereby increasing the plasmonic surface area available for SERS. This red shift improves nanosensor performance in biological samples by reducing background interference. The hydrodynamic diameter of the NCs was 447 ± 5 nm, and the ζ-potential indicated a negative interfacial charge of −28.9 ± 5.01 mV (Fig. SI-1B-C).

To functionalize the plasmonic NCs, we conjugated them with TPY, a Raman sensor for zinc (Šloufová et al., 2018), forming NCs@TPY. Achieving an optimal TPY monolayer for zinc sensing was critical, as TPY density on the plasmonic surface directly influenced the Raman signal (Xiao et al., 2023). Excessive TPY coverage could alter its molecular structure and Raman signature, while insufficient coverage would reduce sensitivity. As shown in Fig. SI–1D, the TPY Raman signal increased with conjugation time, reaching a plateau at 24 h. Likewise, higher TPY concentrations correlated with stronger signals. Based on these findings, we determined that a 24-h reaction time and a TPY concentration of 500 μM were optimal, aligning with previous results (Zhou et al., 2024). While we maintained the same TPY concentration and conjugation time as reported, the increased plasmonic surface led to a higher TPY density. This increase enhanced TPY crystallinity and irradiation efficiency, improving the Raman probe signal.

Given the intended use of the nanosensor in intracellular sensing, it is worth noting that we have exhaustively demonstrated *in vitro* and *in vivo* (Xu et al., 2025; Zamora-Pérez et al., 2025) that our ~450 nm NCs are readily internalised and biocompatible. Extensive multi-modal imaging has shown that nanocapsules of identical size and chemistry accumulate in lysosomes within 2–4 h. Confocal/TEM data (Kastl et al., 2013) were complemented by cryo-soft X-ray tomography in (Xiao et al., 2023; Zamora-Perez et al., 2022), yielding 30 nm-resolution 3-D reconstructions that reveal intact capsules inside endo-lysosomal vesicles without perturbing organelle morphology. The same studies determined an *in vitro* IC_{50} of 4000 pmol L^{-1} for NCs@TPY (Zamora-Perez et al., 2022). The present work employs just 0.072 pmol L^{-1}, over 50.000-fold below this toxicity threshold, providing a very large safety window. Moreover, intravenous administration of the same Au@SiO_2 platform in Balb/c mice caused no clinical, biochemical or histopathological alterations for up to 28 days (Xu et al., 2025). In a second study, intratumoural or peritumoural delivery of the capsules for photothermal ablation of chemoresistant melanoma eradicated tumours without systemic toxicity or organ damage and showed only trace renal clearance of laser-fragmented debris (Zamora-Pérez et al., 2025). Together, these independent datasets confirm efficient internalisation and exceptional biocompatibility of the ~500 nm capsules at the dose used here.

Also important for biosensors is to demonstrate their stability across different pH conditions. Biological environments exhibit a range of pH levels and ionic strengths that can influence colloidal stability and sensing performance (García-Algar et al., 2017; Xiao et al., 2023). To assess these effects, we incubated the nanosensor in solutions with pH values ranging from 3 to 9, which are relevant for biomedical applications (Nazarenus et al., 2015). While the TPY signal exhibits only minimal changes with pH, slight variations in peak intensities and potential shifts in peak positions are observed in the SERS spectra (Fig. 1C). These fluctuations suggest that the interaction of TPY with its environment may be influenced by pH, likely due to changes in its protonation state or molecular conformation. As with any pH-sensitive Raman probe, TPY can undergo protonation or deprotonation at different pH levels, leading to modifications in its electronic structure, bond vibrations, and molecular dipole moment, all of which can impact the SERS spectrum. Fig. 1C shows that the highest intensity is observed at pH 5 thus suggesting an optimal molecular configuration for optimal electronic resonance state where charge transfer is maximized. Even though TPY is covalently attached to the nanostructure, pH fluctuations might induce subtle molecular reorientation. Such changes could affect the angle at which TPY interacts with the plasmonic field, thereby influencing the surface-enhanced electromagnetic coupling and ultimately causing variations in intensity.

Although pH effects do not significantly alter the NCs@TPY SERS signal, they could complicate direct zinc quantification in biological environments. To compensate for pH-induced variations, we regularly employ a ratiometric approach using an internal Raman reference peak (insensitive). Additional strategies we have used to mitigate pH interference, include establishing reliable calibration curves to isolate pH effects from the analyte response, or designing a dual-mode sensor (Xiao

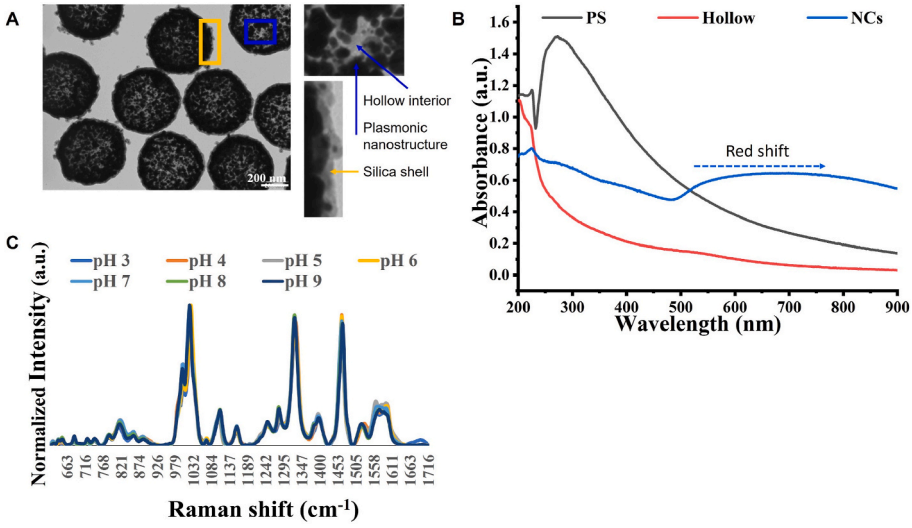

Fig. 1. The zinc nanosensor (NCs@TPY). (A) Electron micrograph of gold (Au)-overgrown nanocapsules (NCs). The NCs consist of a Layer-by-Layer (LbL), a silica (SiO_2) coating and Au seeds that have been grown into nanostructures. However, they have not yet been functionalised with TPY, the Raman probe for zinc. Scale bar: 200 nm. More TEM images are in Fig. SI–1A. **(B)** UV–Vis absorbance spectra of the synthetic stages: PS template (black), Hollow (red) and Au-overgrown NCs (blue). The red shift occurs after Au seeds grow and is therefore with respect to the hollow stage. **(C)** Average SERS spectra of the nanosensors, NCs@TPY, at different pH values (from 3 to 9) demonstrating pH-dependent spectral variations. Each spectrum was normalized by its maxim intensity value. (For interpretation of the references to color in this figure legend, the reader is referred to the Web version of this article.)

et al., 2023).

In this study, we specifically address pH interference in zinc quantification by incorporating pre-calibrated SERS data analysis. We developed a chemometric model that accounts solely for zinc-related variations in the SERS spectra, significantly improving quantification accuracy.

3.2. Enhanced analysis of zinc quantification: univariate vs. multivariate approaches in breast cancer metastasis

Calibration curves are widely used in the biosensor field to establish a quantitative relationship between an analyte's concentration and the corresponding measured signal. Univariate calibration methods are commonly employed due to their simplicity and accessibility, allowing for the prediction of an analyte's concentration in unknown samples based on a standard curve. However, while effective in controlled conditions, univariate methods often introduce errors in complex biological matrices due to spectral interferences, signal variability, and instrument-related noise (Lavín et al., 2018).

To investigate the suitability of univariate calibration for zinc quantification, we dispersed NCs@TPY in zinc-depleted GM supplemented with increasing concentrations of zinc (10^{-4} M to 10^{-12} M). As previously observed by us and others (Zhou et al., 2024; Eremina et al., 2024; Brackx et al., 2020), the intensities of the SERS spectra increased proportionally with zinc concentration (Fig. SI–2A). Notably, four Raman peaks (1021, 1034, 1327, and 1464 cm^{-1}) exhibited high spectral variance (>25 %), indicating sensitivity to changes in zinc levels (Fig. SI–2B). Conversely, peaks at 1108, 1401, 1567, and 1597 cm^{-1} displayed low spectral variance (<25 %), classifying them as zinc-insensitive peaks (Fig. SI–2B) (Xiao et al., 2023).

To normalize signal fluctuations and reduce external influences, we employed a ratiometric approach, comparing the intensity of zinc-sensitive peaks against zinc-insensitive peaks (Zhou et al., 2024; Madhu et al., 2023; Sloan-Dennison et al., 2024). Various combinations were tested to determine the ratio that best correlated with zinc concentration. Among the insensitive peaks, 1108 cm^{-1} was identified as the most stable, corresponding to the C-S vibration of TPY bound to the plasmonic nanostructure. We systematically evaluated different peak ratios, plotting them against the logarithm of zinc concentration (Fig. SI–3). The I_{1021}/I_{1108} ratio demonstrated the strongest linear correlation ($R^2 = 0.934$), leading to the establishment of a calibration curve (Fig. SI–4A).

Fig. SI–4 represents the univariate calibration curve (Fig. SI–4A) obtained in a zinc-depleted cell medium supplemented with exact zinc concentrations ranging from 10^{-4} M to 10^{-12} M and the predicted cellular zinc values as log form (Fig. SI–4B) and as a power of 10 and linear form (Table SI–1). This model establishes a direct relationship between zinc concentration and the SERS signal using a ratiometric method. Although the univariate SERS calibration for Zn^{2+} detection exhibits a linear relationship (slope = 0.0379, intercept = 1.0263) with $R^2 = 0.934$, it suffers from several limitations that undermine its reliability in complex matrices. Systematic errors and baseline spectral fluctuations introduce significant uncertainty, and overlapping Raman peaks from coexisting species can confound the identification of the Zn^{2+} signal. Moreover, the intensity-concentration response may become nonlinear outside the tested range, and inherent SERS substrate variability (hotspot heterogeneity) leads to poor reproducibility. Matrix effects from other bivalent cations (*e.g.,* Ca^{2+} and Mg^{2+}) further interfere *via* competitive binding or background signals. Consequently, despite the high correlation observed under controlled conditions, this univariate approach lacks the robustness required for accurate Zn^{2+} quantification in complex environments.

To address these limitations, we implemented a multivariate regression method using partial least squares (PLS) modeling specifically tailored to each cell type (MCF-7, MDA, LM2, and BrM2) (Fig. 2A–D). The PLS models were developed from SERS spectra obtained from NCs@TPY nanosensors inside tumor cells exposed to zinc-depleted growth medium supplemented with known zinc

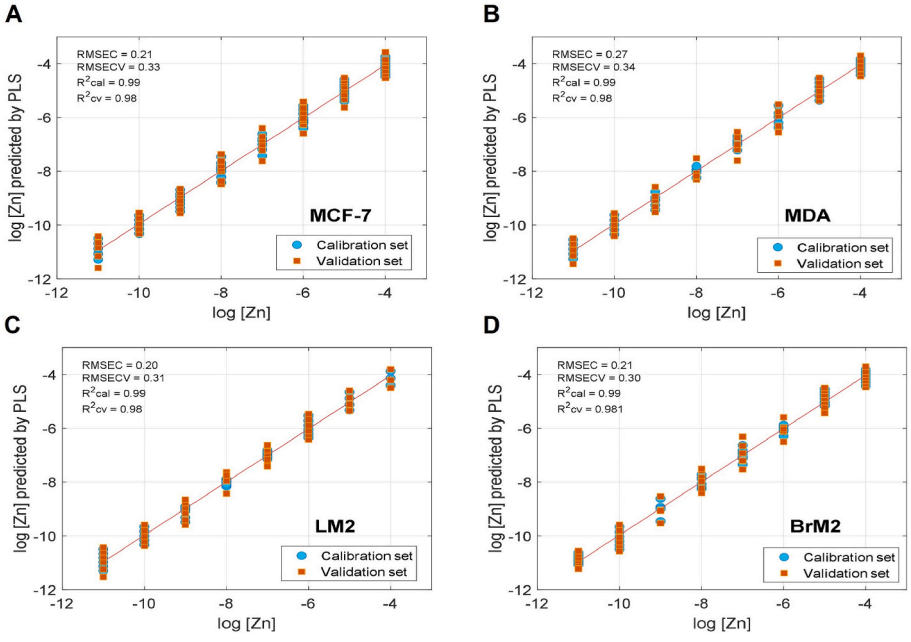

Fig. 2. Cell specific multivariate PLS models for accurate zinc quantification. Partial Least Squares (PLS) regression models used for predicting zinc concentration inside different tumor cell lines following exposure to zinc-depleted GM supplemented with exact zinc concentrations (10^{-4} M to 10^{-11} M) over 2 h. Calibration (blue) and validation (orange) datasets demonstrate the models' performance. Each model's RMSEC, RMSECV, and R^2 values for calibration (R^2_{cal}) and cross-validation (R^2_{cv}) are provided. **(A)** PLS model for MCF-7 cells. **(B)** PLS model for MDA-MB-231 cells. **(C)** PLS model for LM2 (lung metastatic variant). **(D)** PLS model for BrM2 (brain metastatic variant). The high R^2_{cal} and R^2_{cv} values (≥0.98) across all models indicate strong predictive performance, with LM2 showing the lowest RMSEC (0.20), suggesting superior accuracy in zinc uptake modeling. (For interpretation of the references to color in this figure legend, the reader is referred to the Web version of this article.)

A

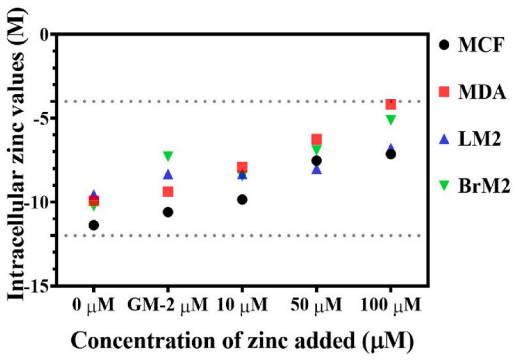

B

$C_{Zn^{2+}(added)}$	$C_{Zn^{2+}(predicted)}$			
	MCF-7	MDA	LM2	BrM2
0 μM	4.2 pM	120 pM	280 pM	58 pM
GM-2 μM	25 pM	430 pM	4.7 nM	51 nM
10 μM	0.14 nM	12 nM	4.8 nM	3.5 nM
50 μM	30 nM	560 nM	9.8 nM	120 nM
100 μM	72 nM	68 μM	160 nM	7.6 μM

Fig. 3. Intracellular zinc concentrations in breast cancer cells following zinc depletion and supplementation. Cells were exposed to different zinc conditions: basal conditions (GM-2 μM, regular culture medium containing 2 μM zinc), zinc depletion (0 μM), and zinc supplementation (10, 50, and 100 μM). Cells were incubated with NCs@TPY for 24 h, and SERS data were recorded. Zinc values were predicted using PLS models for each cell type (Fig. 2A–D). Data are shown for MCF-7 (black), MDA (red), LM2 (blue), and BrM2 (green). The predicted values are presented **(A)** in a log form and **(B)** as a linear value (standard decimal form). See Table SI–2 for the power of 10 form of the zinc values. The figure highlights the concentration-dependent increase in intracellular zinc across all cell lines. (For interpretation of the references to color in this figure legend, the reader is referred to the Web version of this article.)

concentrations (10^{-4} M to 10^{-12} M) over 2 h. Before model development, the SERS spectra were preprocessed using a Savitzky-Golay smoothing filter with a window size of 25 data points and a second-order polynomial fit to reduce noise in the spectral data. In addition, the SERS spectra were autoscaled (refers to subtracting the mean and dividing by the standard deviation for each variable across the calibration set) to prevent variables with higher absolute intensity from dominating the model. The optimal number of latent variables (LVs) was determined by ten-fold cross-validation.

The regression plots of PLS-predicted *versus* actual zinc concentrations (Fig. 2A–D) revealed excellent linearity with R^2 values exceeding 0.98 for calibration and 0.99 in cross-validation. In general terms, for all models, the root mean square error of calibration (RMSEC) and cross-validation of (RMSECV) are comparable, confirming the models' robustness. Model complexity, expressed through the number of LVs, was tailored to the spectral complexity of each cell type, with 5 LVs for MCF-7, 6 for MDA, 9 for LM2, and 7 for BrM2.

The individual PLS models also show distinct performance patterns aligned with each cell type's biological characteristics. Fig. 2A shows the PLS model for MCF-7 cells, built with a lower number of LVs, which had an R^2 of 0.985 and an RMSEC of 0.264. Although the model demonstrates strong linearity, it is the model with the higher prediction errors which indicate lower predictive robustness and suggest greater variability in zinc uptake. This may be attributed to subtle biological fluctuations in zinc homeostasis, lower intracellular zinc levels, or weaker SERS signal intensity, consistent with the non-metastatic, more regulated phenotype of MCF-7 cells. Fig. 2B represents the PLS model for MDA, also built with low LVs, with an improved R^2 of 0.989 and a lower RMSEC of 0.241, indicating stronger zinc uptake predictability. Given that MDA is a highly aggressive and metastatic cancer cell line, this suggests increased zinc transporter activity, likely due to its need for higher zinc levels to support rapid proliferation and invasion (Chandler et al., 2016).

Fig. 2C corresponds to LM2 cells, a lung metastatic variant, which has an R^2 of 0.989 and the lowest RMSEC (0.214) and RMSECV (0.293) among all models. Despite requiring the largest number of LVs to capture more complex spectral patterns, this model's high precision suggests that LM2 cells maintain a tightly regulated zinc uptake mechanism, possibly optimized for survival in the lung metastatic environment (Ramchandani et al., 2021). Finally, Fig. 2D depicts the PLS model for BrM2 cells, a brain metastatic variant, with the highest R^2 (0.990) and an RMSEC of 0.228, using 7 LVs. The larger discrepancy between calibration and cross-validation errors indicates more heterogeneous intracellular zinc handling. This aligns with the biological complexity of brain metastases, where tumor cells exploit neuronal pathways and zinc-dependent signaling mechanisms, leading to more dynamic and variable zinc uptake in response to extracellular zinc availability (Kuett et al., 2025).

Overall, zinc uptake appears to follow a metastatic gradient, with MCF-7 exhibiting the lowest and most variable intracellular zinc uptake, MDA showing increased uptake, LM2 having the most predictable and tight regulation, and BrM2 displaying the highest intracellular zinc dependency. Among the models, the PLS model for LM2 (Fig. 2C) exhibits the best predictive performance (lowest RMSEC), whereas BrM2 (Fig. 2D) demonstrates the highest zinc dependency, reinforcing the concept that zinc transport plays a key role in breast cancer metastasis. These finding suggest that targeting zinc homeostasis could be a promising therapeutic strategy, particularly for brain and lung metastatic tumours, where zinc dependent pathways may be crucial for cancer cell survival and adaptation.

Compared to the univariate ratiometric approach, PLS models demonstrated significantly greater reliability for zinc quantification, even in the presence of potential interfering bications (next section). By leveraging the entire spectral profile, PLS captures subtle signal variations and compensates for matrix effects that can confound univariate methods. While ratiometric analyses are simpler, they are more prone to errors arising from peak fluctuations, baseline drift, and interference from other bications, ultimately limiting their accuracy and reproducibility (Kościelniak and Wieczorek, 2016). In contrast, the multivariate approach integrates zinc-specific spectral information alongside matrix-related variations, minimizing the impact of external factors and improving predictive robustness.

These findings underscore the critical value of adopting multivariate calibration strategies for precise intracellular zinc measurements, particularly in dynamic and heterogeneous systems such as living cells, where high accuracy and reproducibility are essential.

3.3. Ensuring specificity for zinc quantification and avoiding a crosstalk from other bivalent cations with multivariate PLS regression

Accurate intracellular zinc quantification is critical for understanding its role in cellular function, signaling, and disease pathology. However, achieving specificity in zinc detection is challenging due to interference from other physiologically relevant bivalent cations, such as Ca^{2+} and Mg^{2+}, which are present at substantial concentrations in cellular environments. Traditional univariate calibration methods, particularly those based on single-wavelength intensity measurements, are prone to inaccuracies caused by overlapping spectral signals, competitive binding, and complex matrix effects.

To address these limitations, this study employs PLS regression as a robust multivariate technique. Unlike ratiometric methods that assume a direct correlation between a single spectral feature and zinc concentration, PLS regression leverages the entire spectral dataset rather than relying on individual peak intensities. PLS regression decomposes spectral data into LVs that capture the dataset's most significant sources of variation. These LVs represent a combination of spectral features associated with zinc concentration and potential interferents, such as

Ca^{2+} and Mg^{2+}. By modeling the covariance between the spectral data and known zinc concentrations, PLS regression identifies patterns that correlate specifically with zinc, even amidst interference signals.

In biological systems, Ca^{2+} and Mg^{2+} can influence SERS signal intensities through ionic interactions and competitive binding to the nanosensor, thereby acting as interferents in zinc quantification. However, PLS regression inherently accounts for these effects by modeling the entire spectral response rather than relying on fixed peak ratios. Additionally, the spectral region affected by Zn^{2+} binding can exhibit subtle shifts in peak positions and relative intensities. These changes are captured as global spectral trends by the PLS regression, enhancing the robustness and accuracy of the mode and allowing for accurate zinc quantification.

As we proved in the previous section, we developed reliable and robust PLS models (Fig. 2A-D). They exhibit a strong predictive power, with calibration (R^2c) and cross-validation (R^2cv) coefficients exceeding 0.98 and 0.99, respectively and a close agreement between RMSEC and RMSECV. This robustness demonstrates that the method does not overfit specific experimental conditions but rather captures fundamental zinc-related spectral variations, making it applicable across diverse cellular contexts where Ca^{2+} and Mg^{2+} levels fluctuate.

The advantages of developing an intracellular zinc PLS regression model (see next section) ensure that the detected signal responds to Zn^{2+} even in the presence of competing metal ions. It also provides improved accuracy in physiologically relevant conditions where Zn^{2+}, Ca^{2+}, and Mg^{2+} coexist at varying concentrations. Additionally, it offers greater robustness for quantitative zinc analysis, particularly in heterogeneous biological samples where matrix effects are non-negligible. In contrast, ratiometric univariate calibration remains vulnerable to misinterpretation due to its reliance on a single spectral ratio, which may be altered by environmental fluctuations or non-specific interactions with other biomolecules.

In conclusion, this study establishes PLS regression as a superior methodology for intracellular zinc quantification, effectively minimizing crosstalk from Ca^{2+} and Mg^{2+} while enhancing specificity and accuracy. This approach represents a valuable tool for future research into zinc homeostasis, signaling pathways, and disease-associated dysregulations, where precise quantification is essential for understanding zinc's role in cellular function and pathology.

3.4. Quantification of the intracellular labile zinc amount after external zinc addition to metastatic and low metastatic cells

In this study, we investigate whether zinc dyshomeostasis correlates with metastatic potential in breast cancer cells. Four breast-cancer cell lines that span a metastatic spectrum were analyzed: the low metastatic ER^+/PR^+ MCF-7, the parenteral TNBC MDA, and two organ-tropic derivatives, LM2 (lung) and BrM2 (brain). To explore this correlation, we manipulated zinc levels in these cells, measured intracellular labile zinc, and assessed key pro-metastatic characteristics, including proliferation, migration, and invasiveness.

Labile zinc is estimated to exist in the picomolar range, with even slight deviations linked to cancer progression. Since precise values are unavailable, we first quantified intracellular labile zinc under normal conditions (GM, basal condition, naturally containing 2 μM) before altering zinc levels by depletion or supplementation (zinc-depleted GM supplemented with 0, 10, 50, or 100 μM zinc) (see methods). Cells were incubated with nanosensors for 24 h, and intracellular zinc concentrations were predicted using the chemometric models (Fig. 2). As shown in Fig. 3, increasing extracellular zinc led to a concentration-dependent rise in intracellular labile zinc across all cell types. The predicted values are presented as log form (Fig. 3A) and as linear values (Fig. 3B) and Table SI–2 also shows the predicted values as power of 10.

Under basal growth conditions (GM-2 μM), labile-zinc pools span three orders of magnitude, 25 pM in MCF-7, 430 pM in MDA-MB-231, 4.7 nM in LM2 and 51 nM in BrM2, establishing a clear zinc-level gradient that mirrors their increasing metastatic aggressiveness (Fig. 3B). Notably, MCF-7 cells had the lowest zinc levels, while metastatic cells exhibited higher levels. Among the metastatic cells, those derived from metastatic sites (LM2 and BrM2) had more zinc than MDA. Zinc depletion (0 μM) reduced intracellular zinc in all cell lines, with LM2 and BrM2 showing the most significant drop. The measured values were: MCF-7 (4.2 pM), MDA (120 pM), LM2 (280 pM), and BrM2 (58 pM). Cells derived from the primary tumor (MCF-7 & MDA) were more resistant to zinc depletion than the other lines, maintaining their basal levels more effectively.

Adding zinc (10–100 μM) increased intracellular zinc across all cell lines in a concentration dependent manner, with the highest values recorded at maximal supplementation: MCF-7 (72 nM), MDA (68 μM), LM2 (160 nM), and BrM2 (7.6 μM) (Fig. 3B). Among these, MDA cells exhibited the highest intracellular zinc concentration, while MCF-7 had the lowest. The metastatic cell lines LM2 and BrM2 showed intermediate levels, with BrM2 accumulating more zinc than LM2. Notably, BrM2 responded to increasing extracellular zinc levels, whereas LM2 maintained relatively stable zinc concentrations. This suggests LM2 may possess stronger zinc homeostasis mechanisms compared to the other cell lines.

The observed differences in intracellular zinc levels among various breast cancer cell lines may be linked to their metastatic potential. Notably, metastatic cells derived from primary tumours, such as the MDA cell line, exhibited higher intracellular zinc concentrations compared to low-metastatic MCF-7 cells. This observation aligns with research indicating that the nature of the primary seeding cancer cell influences metastatic properties, including growth and dissemination capabilities (Fares et al., 2020). Furthermore, cell lines originating from metastatic sites, like LM2 and BrM2, displayed intermediate zinc levels, suggesting that the metastatic microenvironment may also play a role in modulating zinc homeostasis. The metastatic potential of breast cancer cells varies depending on their origin, highlighting the complex interplay between tumor origin and metastatic behavior (Jin et al., 2020). Research indicates that cell lines derived from metastatic sites often exhibit higher metastatic potential than those from primary tumours. However, some primary tumor-derived cell lines, particularly those from tumours known to metastasize in patients, also demonstrate significant metastatic capabilities (Jin et al., 2020). This suggests that metastatic potential of breast cancer cells can be encoded early in tumor development, but cells from metastatic sites may have undergone additional adaptations enhancing their ability to colonize distant organs.

The variability in metastatic potential among cancer cells appears to be cancer-type dependent. For instance, in ovarian cancer, cells from primary tumours often exhibit significant metastatic capabilities, spreading through mechanisms such as exfoliation of cancer cells from the primary site. Similarly, skin metastases, though uncommon, have been observed in ovarian cancer patients, indicating the aggressive nature of primary tumor cells in certain cases (Mukherjee et al., 2022). Conversely, in cancers like pancreatic ductal adenocarcinoma (PDAC), metastasis frequently involves dissemination to distant organs, with the liver being the most common metastatic site. This suggests that the metastatic potential of cancer cells may vary depending on the type of cancer and the origin of the metastatic cells (Houg and Bijlsma, 2018).

In conclusion, metastatic breast cancer cells derived from the primary tumor (MDA) contained the highest zinc levels, whereas low-metastatic MCF-7 cells had the lowest, differing by approximately three orders of magnitude. BrM2 cells exhibited zinc accumulation in response to supplementation, whereas LM2 maintained stable intracellular zinc levels regardless of extracellular zinc fluctuations. These insights underscore the importance of considering both the origin of cancer cells and their microenvironment when investigating factors such as zinc dyshomeostasis that may influence metastatic progression. Furthermore, these findings suggest a potential correlation between zinc homeostasis and metastatic behavior in breast cancer cells.

3.5. Zinc-homeostasis plasticity drives proliferative advantage along the metastatic continuum of breast cancer

Having quantified how each cell line handles labile zinc (Fig. 3), we next asked how these zinc loads influence proliferation. Metastatic breast cancer cells often exhibit higher proliferation rates compared to their non-metastatic counterparts, contributing to their aggressive behavior and colonization of new tissues. Early-stage metastatic breast cancer cells display a stem-like gene expression signature, which is linked to increased proliferation and differentiation into more aggressive forms (Lawson et al., 2015). Because zinc is an essential trace element influencing cancer cell proliferation by affecting DNA synthesis, cell cycle progression, and key signaling pathways (Alam and Kelleher, 2012), we examined whether disrupting zinc homeostasis, either by depletion or by acute overload, modulates proliferation in proportion to metastatic aggressiveness.

Disrupting zinc homeostasis produced clear, line-specific effects on cell division that paralleled metastatic aggressiveness (Fig. 4). Zinc was added to the cultures at day 0 (D0), and intracellular labile Zn^{2+} concentrations (C_{Zn2+}, Fig. 3B) were quantified immediately before addition (D0, baseline) and used as initial points for the ensuing four-day exposure. This single supplementation created intracellular Zn^{2+} pools that differed by up to five orders of magnitude, from picomolar under depletion to low-micromolar at the highest external dose, yet only the low-metastatic MCF-7 cells were unable to buffer these extremes. When C_{Zn2+} fell to 4 pM or rose modestly to 0.14 nM, MCF-7 proliferation slowed by ~20 % (Zinc-Imbalance Index, ZII ≈ +0.23; Table 1). Growth partially recovered at higher doses (30–72 nM), implying a very narrow "optimal" window for this ER^+ line.

The triple-negative parental MDA-MB-231 (MDA) responded in the opposite direction. Zinc depletion produced a small but reproducible acceleration, and every increase in extracellular zinc drove faster dye dilution until proliferation peaked after continuous exposure to 50 μM (C_{Zn2+} ≈ 560 nM). Only when C_{Zn2+} reached ~68 μM at the 100 μM supplement did growth begin to taper, yielding a strongly negative ZII (−0.38). The lung-tropic LM2 and brain-tropic BrM2 derivatives showed similar zinc-stimulated acceleration, although both tolerated depletion better than MCF-7 and exhibited shallower dose-responses than their MDA progenitor. For each line, plotting ZII against $\log_{10}C_{Zn2+}$ gave highly negative linear correlation coefficients (r = −0.94 MCF-7, -0.98 MDA, −0.89 LM2, -0.75 BrM2), demonstrating that larger intracellular zinc excursions preferentially benefit the more metastatic cells. Qualitatively, the ability either to exploit excess zinc or to endure scarcity increases in the order MCF-7 < LM2 ≈ BrM2 < MDA, mirroring their metastatic competence.

These findings reveal a continuum of zinc-homeostasis plasticity. Low-metastatic MCF-7 cells function only within a narrow zinc range and are compromised by both shortage and oversupply, whereas highly metastatic TNBC derivatives leverage elevated Zn^{2+} to accelerate division and are largely indifferent to depletion. This gradient likely reflects progressive up-regulation of zinc transporters, metallothioneins and buffering sites that expand the labile pool without triggering toxicity. Such adaptations would simultaneously fuel proliferation, zinc is required for DNA synthesis, cell-cycle kinases and PI3K/AKT signalling, and shield the cells from the oxidative and proteostatic stress that accompanies metastatic colonization.

Therapeutically, the data point to a double opportunity: modest chelation could selectively arrest zinc-sensitive ER^+ tumours, whereas inhibitors of ZIP importers or metallothionein induction might undermine the "zinc addiction" of aggressive triple-negative clones. Whether

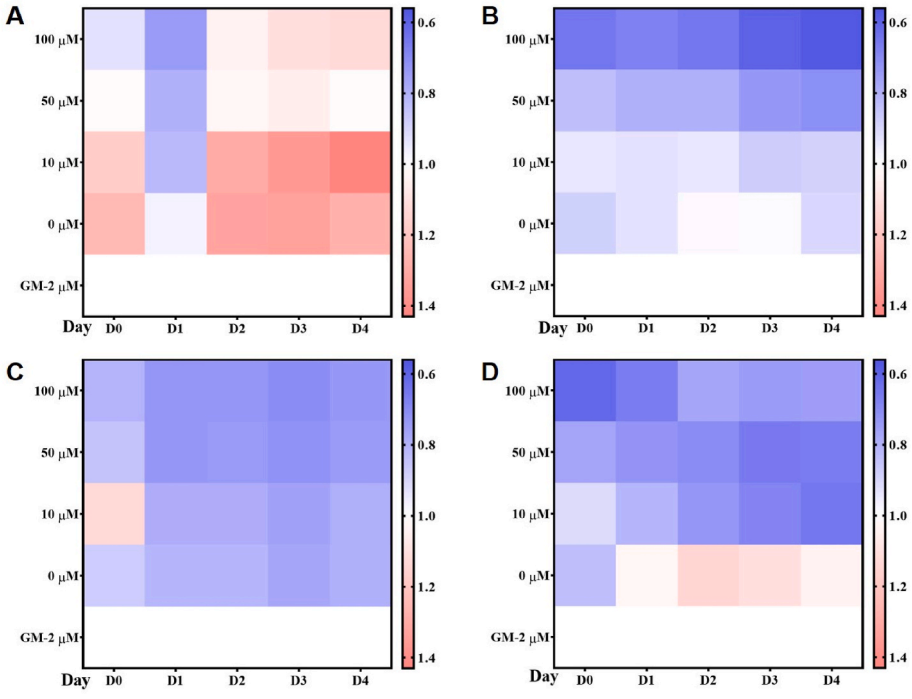

Fig. 4. Zinc dependence of proliferation in breast cancer cell lines that differ in metastatic potential. The proliferative response of **(A)** MCF-7 (low-metastatic), **(B)** MDA (metastatic, parenteral), **(C)** LM2 (lung-tropic derivative), and **(D)** BrM2 (brain-tropic derivative) cells was monitored from day 0 (D0) to day 4 (D4) after exposure to graded extracellular zinc concentrations: 0 (zinc-depleted), GM-2 μM (reference, white row), and supplementation with 10, 50, 100 μM. Cells were labelled with a fluorescent proliferation dye, where increased proliferation results in dye dilution and a reduced fluorescence signal. The fluorescence ratio of daughter/parent population was calculated and normalized to the GM-2 μM baseline, yielding a proliferation ratio (R): R = 1 (white) = growth identical to GM-2 μM; R < 1 (blue) = faster proliferation than GM-2 μM; R > 1 (pink) = slower proliferation than GM-2 μM. The color bar spans the full data range (0.56–1.43). Lower ratios (deep blue) therefore correspond to higher proliferation rates. The maps suggest that zinc modulates proliferation in a concentration-dependent manner, with variations across different metastatic potentials. (For interpretation of the references to color in this figure legend, the reader is referred to the Web version of this article.)

Table 1
Zinc-Imbalance Index (ZII) and its correlation with intracellular Zn^{2+}. Cells were cultured for 4 days in medium containing 0, 10, 50 or 100 μM Zn^{2+}. ZII (average growth change relative to the GM-2 μM baseline) and the Pearson correlation coefficient (r) between ZII and $\log_{10}$-transformed intracellular labile Zn^{2+} (values from Fig. 3B) are listed for each line.

	MCF-7		MDA		LM2		BrM2	
C_{Zn2+}(added)	ZII	r	ZII	r	ZII	r	ZII	r
0 μM (depletion)	0.225	−0.936	−0.049	−0.976	−0.201	−0.892	0.078	−0.752
10 μM	0.223		−0.094		−0.219		−0.282	
50 μM	−0.031		−0.242		−0.268		−0.314	
100 μM	0.004		−0.378		−0.277		−0.267	

zinc plasticity merely marks, or actively drives, metastatic progression now merits testing with live-cell Zn^{2+} reporters, transporter knock-outs and invasion assays. Nonetheless, the present results establish labile-zinc handling as a quantifiable and exploitable vulnerability along the metastatic trajectory of breast cancer.

3.6. Zinc modulates migration and invasion of metastatic breast cancer cells via a line-specific biphasic switch

Our data reveals a clear biphasic (inverted-U) control of metastatic behaviour by labile zinc. Although the precise relationship between intracellular Zn^{2+} and metastatic behaviour is cell line-specific, the overall pattern is conserved across all metastatic models (Fig. 5). Migration, invasion and proliferation peak when cytosolic Zn^{2+} resides within a narrow 3.5 nM–560 nM corridor and decline once it exceeds the line-specific ceiling (≈160 nM in LM2, ≈7.6 μM in BrM2, ≈68 μM in MDA; Figs. 4 and 5). These limits were quantified with our 8-log NCs@TPY nanosensor/PLS platform, which detects Zn^{2+} down to 4.2 pM, ~100-fold more sensitive than previous intracellular SERS probes.

Zinc homeostasis is implicated in tumor progression and metastasis, where it can either promote or inhibit migration and invasion depending on concentration and cellular context (Jin et al., 2020). Metastasis is a complex, multi-step process, with migration and invasion being two critical components (Wu et al., 2021). To investigate how zinc imbalance influences these behaviours, we seeded the breast cancer cell lines in trans-well inserts and exposed them to different zinc concentrations (0 μM, GM-2 μM, 10 μM, 50 μM, 100 μM) for 48 h. Migrated or invaded cells were stained with crystal violet, converted to cell numbers *via* a standard curve (Fig. SI-6) and plotted as % migration/invasion (Fig. 5). Consistent with previous findings (Rosman et al., 2008), the non-invasive breast cancer cell line MCF-7 exhibited negligible migration and invasion, which resulted in negative values (Figs. SI–7, SI-8, and SI-9) (Haase and Rink, 2014). Including MCF-7 would therefore distort Fig. 5; we focused on the metastatic lines (MDA, LM2, BrM2) where zinc-induced effects are measurable.

Under regular culture conditions (GM-2 μM), the metastatic cells from the primary tumor (MDA) displayed greater migratory ability than those from metastatic sites (LM2 and BrM2), whereas LM2 and BrM2 were more invasive (Fig. SI–9B). Interestingly, MDA cells were more sensitive to zinc fluctuations, while LM2 and BrM2 were comparatively resistant to zinc-induced alterations, suggesting a potential adaptation of these metastatic cells to zinc homeostasis (Fig. 5).

The migration of all metastatic cell lines increased in a concentration-dependent manner up to 50 μM zinc, after which it declined at 100 μM (Fig. 5A). In MDA cells, migration was significantly enhanced at 10 μM (intracellular: 12 nM) and peaked at 50 μM (560 nM; $p < 0.0001$). LM2 and BrM2 followed a similar pattern, with increased migration at 10 μM (4.8 nM for LM2, 3.5 nM for BrM2) and peaking at 50 μM (9.8 nM for LM2, 120 nM for BrM2). At 100 μM zinc supplementation, where intracellular zinc levels reached 68 μM in MDA, 160 nM in LM2, and 7.6 μM in BrM2, migration was significantly reduced across all cell lines, suggesting an inhibitory or toxic effect. Zinc deprivation (0 μM) likewise reduced migration in all metastatic cells, emphasizing the essential role of zinc in maintaining cellular motility (Fig. 5A). In contrast, the GM-2 μM condition (430 pM in MDA, 4.7 nM in LM2, 51 nM in BrM2) did not significantly alter migration, indicating that basal zinc levels alone are insufficient to drive metastatic behavior.

Similar to migration, invasion increased with zinc exposure up to 50 μM before declining at 100 μM (Fig. 5B). MDA cells showed a significant increase in invasion at 10 μM (12 nM) and 50 μM (560 nM). LM2 cells exhibited a more moderate response, with invasion increasing at 10 μM (4.8 nM) and 50 μM (9.8 nM) but with less pronounced differences compared to migration, suggesting that LM2 cells may be more resistant to zinc-induced changes in invasion. BrM2 cells followed the same trend, reaching a maximum intracellular zinc concentration of 120 nM at 50 μM, which correlated with increased invasion. However, their invasiveness was less affected by zinc compared to migration, suggesting a potential threshold where zinc influences migratory ability more than invasive potential.

Across all metastatic lines, maximal migration/invasion occurred when intracellular Zn^{2+} rose into the nanomolar regime (≈9.8–560 nM), whereas low-micromolar levels consistently suppressed both processes (Fig. 5). These values coincide with two zinc-dependent, motility-limiting steps: (i) ZIP6/ZIP10 influx saturates at ~0.3–1 μM free Zn^{2+}, activating STAT3-EMT signalling (Taylor et al., 2016); (ii) Matrix-metalloproteinases 2/9 are half-maximally activated at 0.5–5 μM

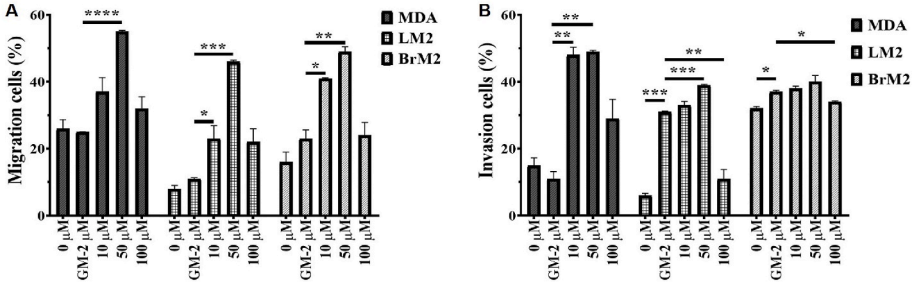

Fig. 5. Zinc influences the migration and invasiveness of metastatic breast cancer cells. (A) Migration and **(B)** invasion of metastatic breast cancer cell lines (MDA, LM2, and BrM2) under varying zinc concentrations (0, GM-2 μM, 10 μM, 50 μM, 100 μM). Data represent the mean ± standard deviation (StDev) from at least two independent experiments. Statistical significance was assessed using a two-tailed Student's t-test, where * $p < 0.05$, ** $p < 0.01$, *** $p < 0.001$, and **** $p < 0.0001$.

Zn^{2+}. The 560 nM (MDA) point we observe therefore marks the cross-over where both transport and protease activity are both maximized. Excess Zn^{2+} saturates transporters, disrupts proteostasis and dampens MMP expression, explaining high-dose inhibition (Vogel-González et al., 2021).

At 100 μM zinc, the increased intracellular levels (68 μM in MDA and 7.6 μM in BrM2) correlate with reduced invasion. LM2's smaller rise (160 nM) and milder inhibition further underscore its zinc resilience.

These results are aligned with those observed in proliferation studies (Fig. 4), where LM2 and BrM2 cells showed resistance to alterations in zinc levels, particularly at 50 μM, while MDA cells remained the most sensitive to zinc fluctuations. The differential responses among MDA, LM2, and BrM2 cells may be attributed to their distinct metastatic origins. MDA cells originate from the primary tumor and may require broader zinc swings to facilitate metastasis to distant organs (Chandler et al., 2016; Verma et al., 2024), while LM2 and BrM2 have adapted to zinc-restricted lung and brain niches (Jiang et al., 2017).

Zinc is also a co-factor for MMPs, which degrade extracellular matrix components to facilitate invasion (Kuett et al., 2025). Moderate Zn^{2+} boosts MMP activity, while excess disrupts signaling, induces oxidative stress and represses MMP genes, reinforcing the biphasic model *i.e.,* moderate intracellular levels enhance metastatic potential, whereas excessive zinc may impair essential cellular processes required for tumor progression.

In brief, zinc modulates the migration and invasion of metastatic breast cancer cells in a concentration-dependent and cell-specific manner. Moderate supplements (10 μM and 50 μM) elevate intracellular Zn^{2+} into the pro-metastatic nanomolar window, whereas deprivation or overload suppresses motility. MDA responds more strongly while LM2 and BrM2 exhibited relative resistance, particularly in invasion. Pushing Zn^{2+} below ~10 nM or above each line's ceiling could therefore restrain metastasis. Further research should focus on the molecular mechanisms by which zinc influences MMP regulation, EMT, and oxidative stress, as these processes may determine the balance between metastasis promotion and inhibition.

4. Conclusions

This study delivers two interconnected advances. First, by coupling a hollow $Au@SiO_2$ nanocapsule functionalised with terpyridine (NCs@TPY) to cell-specific partial-least-squares models, we establish an 8-log analytical window for live-cell labile Zn^{2+} sensing. The full-spectrum, multivariate approach achieved a low cross-validation error and quantifies intracellular zinc from roughly 10^{-9} M up to 10^{-4} M, an improvement of about two orders of magnitude over previous intracellular SERS probes, and far less vulnerable to Ca^{2+}/Mg^{2+} cross-talk than the conventional univariate 1021/1108 cm^{-1} ratio.

Second, the sensor uncovers a biphasic "metastatic switch" governed by labile zinc. Basal zinc pools already mirror intrinsic aggressiveness, rising from 25 pM in low-metastatic MCF-7 cells to 51 nM in brain-tropic BrM2 cells. When extracellular zinc is supplemented, migration, invasion and proliferation in all metastatic lines climb sharply as intracellular Zn^{2+} enters the ≈10 nM–0.6 μM band and then collapse once zinc exceeds each line's ceiling (≈7 μM for BrM2 and ≈70 μM for MDA), a regime where transporter saturation and zinc-dependent MMP dysregulation likely dominate. Tumour origin modulates this response: primary-tumour-derived MDA cells are highly zinc-sensitive, reaching maximal metastatic traits at ~0.6 μM Zn^{2+}, whereas lung- and brain-derived variants (LM2, BrM2) tolerate zinc stress better. BrM2 still responding strongly at ~120 nM and LM2 plateauing at ~10 nM and showing the greatest resistance. MCF-7 remains largely non-migratory, exhibiting only a modest proliferation boost at higher zinc.

Taken together, these results demonstrate that zinc dyshomeostasis is not merely a marker but a quantitative driver of metastatic behaviour. Because the nanocapsule architecture can accommodate other Raman ligands, the platform is readily extendable to multiplex ion or redox imaging in live tumours and patient-derived organoids. Strategically pushing cytosolic Zn^{2+} below ~10 nM or above ~5–70 μM (line specific), either by buffering or by targeting zinc transporters, emerges as a tangible avenue for restraining metastatic dissemination in breast cancer and, potentially, other solid tumours.

CRediT authorship contribution statement

Ting Zhou: Writing – review & editing, Methodology, Investigation, Formal analysis. **Suliany Rodríguez-Barrios:** Writing – review & editing, Methodology, Investigation, Formal analysis. **Itziar Ruisánchez:** Writing – review & editing, Methodology, Formal analysis, Conceptualization. **Pilar Rivera-Gil:** Writing – review & editing, Writing – original draft, Supervision, Resources, Project administration, Methodology, Investigation, Funding acquisition, Formal analysis, Conceptualization.

Funding sources

PRG acknowledges the Spanish Ministry of Science, Innovation and Technology (AEI-PID2022-140423NB-100/AEI/10.13039/501100011033 and CNS2023 - 143700) for funding.

TZ. and PRG appreciate the financial support from the China Scholarship Council (CSC) by a State Scholarship Fund (NSCIS no. 202008350121).

With the support of the Department of Research and Universities of the Generalitat of Catalonia in the Chemometrics and Sensorics for Analytical Solutions Research Group, CHEMOSENS (Code: 2021 SGR 00705).

Declaration of competing interest

The authors declare that they have no known competing financial interests or personal relationships that could have appeared to influence the work reported in this paper.

Appendix A. Supplementary data

Supplementary data to this article can be found online at https://doi.org/10.1016/j.bios.2025.117897.

Data availability

supporting information file.

References

Akhlaghipour, I., Moghbeli, M., 2024. Eur. J. Pharmacol. 982, 176966.
Alam, S., Kelleher, S.L., 2012. Nutrients 4, 875–903.
Brackx, G., Guinoiseau, D., Duponchel, L., Gélabert, A., Reichel, V., Zrig, S., Meglio, J.-M. D., Benedetti, M.F., Gaillardet, J., Charron, G., 2020. Sci. Rep. 10, 1883.
Bro, R., Smilde, A.K., 2014. Anal. Methods 6, 2812–2831.
S. Carregal Romero, J. M. Montenegro Martos, W. Parak and P. Rivera_Gil, Front. Pharmacol., DOI:10.3389/fphar.2012.00070.
Chandler, P., Kochupurakkal, B.S., Alam, S., Richardson, A.L., Soybel, D.I., Kelleher, S.L., 2016. Mol. Cancer 15, 2.
Colvin, R.A., Holmes, W.R., Fontaine, C.P., Maret, W., 2010. Met. Integr. Biometal Sci. 2, 306–317.
dos Santos, D.P., Sena, M.M., Almeida, M.R., Mazali, I.O., Olivieri, A.C., Villa, J.E.L., 2023. Anal. Bioanal. Chem. 415, 3945–3966.
Eremina, O.E., Yarenkov, N.R., Bikbaeva, G.I., Kapitanova, O.O., Samodelova, M.V., Shekhovtsova, T.N., Kolesnikov, I.E., Syuy, A.V., Arsenin, A.V., Volkov, V.S., Tselikov, G.I., Novikov, S.M., Manshina, A.A., Veselova, I.A., 2024. Talanta 266, 124970.
Fares, J., Fares, M.Y., Khachfe, H.H., Salhab, H.A., Fares, Y., 2020. Signal Transduct. Targeted Ther. 5, 1–17.
Finney, L.A., O'Halloran, T.V., 2003. Science 300, 931–936.
García-Algar, M., Tsoutsi, D., Sanles-Sobrido, M., Cabot, A., Izquierdo-Roca, V., Gil, Habil P.R., 2017. ChemistrySelect 2, 8115–8121.
Haase, H., Rink, L., 2014. BioFactors Oxf. Engl. 40, 27–40.
Houg, D.S., Bijlsma, M.F., 2018. Mol. Cancer 17, 95.
Jiang, J., Wang, K., Chen, Y., Chen, H., Nice, E.C., Huang, C., 2017. Signal Transduct. Targeted Ther. 2, 1–12.

Jin, X., Demere, Z., Nair, K., Ali, A., Ferraro, G.B., Natoli, T., Deik, A., Petronio, L., Tang, A.A., Zhu, C., Wang, L., Rosenberg, D., Mangena, V., Roth, J., Chung, K., Jain, R.K., Clish, C.B., Vander Heiden, M.G., Golub, T.R., 2020. Nature 588, 331–336.
Kagara, N., Tanaka, N., Noguchi, S., Hirano, T., 2007. Cancer Sci. 98, 692–697.
Kantner, K., Ashraf, S., Carregal-Romero, S., Carrillo-Carrion, C., Collot, M., del Pino, P., Heimbrodt, W., De Aberasturi, D.J., Kaiser, U., Kazakova, L.I., Lelle, M., de Baroja, N.M., Montenegro, J.M., Nazarenus, M., Pelaz, B., Peneva, K., Gil, P.R., Sabir, N., Schneider, L.M., Shabarchina, L.I., Sukhorukov, G.B., Vazquez, M., Yang, F., Parak, W.J., 2015. Small 11, 896–904.
Kastl, L., Sasse, D., Wulf, V., Hartmann, R., Mircheski, J., Ranke, C., Carregal-Romero, S., Martínez-López, J.A., Fernández-Chacón, R., Parak, W.J., Elsasser, H.-P., Rivera_Gil, P., 2013. ACS Nano 7, 6605–6618.
Kneipp, J., Kneipp, H., Wittig, B., Kneipp, K., 2010. J. Phys. Chem. C 114, 7421–7426.
Kościelniak, P., Wieczorek, M., 2016. Anal. Chim. Acta 944, 14–28.
Kuett, L., Bollhagen, A., Tietscher, S., Sobottka, B., Eling, N., Varga, Z., Moch, H., de Souza, N., Bodenmiller, B., 2025. Cancer Res. 85, 15–31.
Lavín, Á., Vicente, J.D., Holgado, M., Laguna, M.F., Casquel, R., Santamaría, B., Maigler, M.V., Hernández, A.L., Ramírez, Y., 2018. Sensors 18, 2038.
Lawson, D.A., Bhakta, N.R., Kessenbrock, K., Prummel, K.D., Yu, Y., Takai, K., Zhou, A., Eyob, H., Balakrishnan, S., Wang, C.-Y., Yaswen, P., Goga, A., Werb, Z., 2015. Nature 526, 131–135.
Lee, W., Kang, B.-H., Yang, H., Park, M., Kwak, J.H., Chung, T., Jeong, Y., Kim, B.K., Jeong, K.-H., 2021. Nat. Commun. 12, 159.
Li, W., Zamani, R., Rivera Gil, P., Pelaz, B., Ibáñez, M., Cadavid, D., Shavel, A., Alvarez-Puebla, R.A., Parak, W.J., Arbiol, J., Cabot, A., 2013. J. Am. Chem. Soc. 135, 7098–7101.
Madhu, M., Santhoshkumar, S., Tseng, W.-B., Tseng, W.-L., 2023. Front. Anal. Sci. 3, 1258558. https://doi.org/10.3389/frans.2023.1258558.
Maret, W., 2015. Metallomics 7, 202–211.
Maret, W., 2017. Int. J. Mol. Sci. 18, 2285.
Mukherjee, A., Zhang, H., Ladner, K., Brown, M., Urbanski, J., Grieco, J.P., Kapania, R. K., Lou, E., Behkam, B., Schmelz, E.M., Nain, A.S., 2022. Mol. Biol. Cell 33, ar55.
Nazarenus, M., Abasolo, I., García-Aranda, N., Voccoli, V., Rejman, J., Cecchini, M., Schwartz Jr., S., Rivera_Gil, P., Parak, W.J., 2015. Part. Part. Syst. Char. 32, 991–998.
Nie, S., Emory, S.R., 1997. Science 275, 1102–1106.
Peng, J., Peng, S., Jiang, A., Wei, J., Li, C., Tan, J., 2010. Anal. Chim. Acta 683, 63–68.
Ramchandani, D., Berisa, M., Tavarez, D.A., Li, Z., Miele, M., Bai, Y., Lee, S.B., Ban, Y., Dephoure, N., Hendrickson, R.C., Cloonan, S.M., Gao, D., Cross, J.R., Vahdat, L.T., Mittal, V., 2021. Nat. Commun. 12, 7311.
Ringgit, G., Siddiquee, S., Saallah, S., Mohamad Lal, M.T., 2022. Sci. Rep. 12, 18582.
Rivera-Gil, P., Vazquez-Vazquez, C., Giannini, V., Callao, M.P., Parak, W.J., Correa-Duarte, M.A., Alvarez-Puebla, R.A., 2013. Angew Chem. Int. Ed. Engl. 52, 13694–13698.
Rosman, D.S., Phukan, S., Huang, C.-C., Pasche, B., 2008. Cancer Res. 68, 1319–1328.
Sanles-Sobrido, M., Exner, W., Rodríguez-Lorenzo, L., Rodríguez-González, B., Correa-Duarte, M.A., Álvarez-Puebla, R.A., Liz-Marzán, L.M., 2009. J. Am. Chem. Soc. 131, 2699–2705.
Seyfried, T.N., Huysentruyt, L.C., 2013. Crit. Rev. Oncog. 18, 43–73.
Sloan-Dennison, S., Wallace, G.Q., Hassanain, W.A., Laing, S., Faulds, K., Graham, D., 2024. Nano Converg. 11, 33.
Šloufová, I., Vlčková, B., Mojzeš, P., Matulková, I., Císařová, I., Procházka, M., Vohlídal, J., 2018. J. Phys. Chem. C 122, 6066–6077.
Taylor, K.M., Muraina, I.A., Brethour, D., Schmitt-Ulms, G., Nimmanon, T., Ziliotto, S., Kille, P., Hogstrand, C., 2016. Biochem. J. 473, 2531–2544.
Tsoutsi, D., Sanles-Sobrido, M., Cabot, A., Gil, P.-R., 2018. Curr. Med. Chem. 25, 4638–4652.
Vázquez-Vázquez, C., Vaz, B., Giannini, V., Pérez-Lorenzo, M., Alvarez-Puebla, R.A., Correa-Duarte, M.A., 2013. J. Am. Chem. Soc. 135, 13616–13619.
Verma, S., Giagnocavo, S.D., Curtin, M.C., Arumugam, M., Osburn-Staker, S.M., Wang, G., Atkinson, A., Nix, D.A., Lum, D.H., Cox, J.E., Hilgendorf, K.I., 2024. Cancer Res. Commun. 4, 1655–1666.
Vogel-González, M., Musa-Afaneh, D., Rivera Gil, P., Vicente, R., 2021. Int. J. Mol. Sci. 22, 9188.
Wiklund, S., Nilsson, D., Eriksson, L., Sjöström, M., Wold, S., Faber, K., 2007. J. Chemom. 21, 427–439.
Wu, J., Jiang, J., Chen, B., Wang, K., Tang, Y., Liang, X., 2021. Transl. Oncol. 14, 100899.
Xiao, C., Izquierdo-Roca, V., Rivera-Gil, P., 2023. ACS Mater. Au 3, 164–175.
Xu, R., Martinez-Bosch, Neus, Rivera-Hueto, Francisco, Mulens-Arias, Vladimir, Rubio-Moscardo, Fanny, Javier Conesa, J., Navarro, Pilar, Vicente, Rubén, Rivera-Gil, 2025. J. Drug Target. 33, 143–155.
Zamora-Pérez, P., She, Q., Santos, H.D.A., Conesa, J.J., Iglesias-de la Cruz, M.C., Fernández, N., Jaque, D., Rivera-Gil, P., 2025. J. Mater. Chem. B 13, 9498–9511.
Zamora-Perez, P., Xiao, C., Sanles-Sobrido, M., Rovira-Esteva, M., Conesa, J.J., Mulens-Arias, V., Jaque, D., Rivera-Gil, P., 2022. Acta Biomater. 142, 308–319.
Zhou, T., Vicente, R., Rivera-Gil, P., 2024. ACS Omega 9, 42183–42192.